Check for updates

Electronic and magnetic properties of a black phosphorene/Tl₂S heterostructure with transition metal atom intercalation: a first-principles study†

Yusheng Wang, [iD] *[ac] Xiaoyan Song,[a] Nahong Song,[bc] Tianjie Zhang,[a] Xiaohui Yang,[a] Weifen Jiang[a] and Jianjun Wang[d]

Using density functional theory calculations, the structural, electronic and magnetic properties of a black phosphorene/Tl₂S heterostructure (BP/Tl₂S) and the BP/Tl₂S intercalated with transition metal atoms (TMs) have been detailed investigated. It is demonstrated that the BP/Tl₂S is a type-I van der Waals (vdW) heterostructure with an indirect band gap of approximately 0.79 eV. The BP/Tl₂S experiences a transition from type-I to type-II when various strains are applied. In addition, the BP/Tl₂S intercalated with TMs (TM-BP/Tl₂S) exhibits various kinds of meaningful electronic and magnetic properties. Several TM-BP/Tl₂S systems are still non-magnetic ground states and six TM-BP/Tl₂S (Ti-, V-, Cr-, Mn-, Fe-, Tc-) systems are ferromagnetic. Interestingly, three TM-BP/Tl₂S (V-, Cr-, Mn-) systems display half-metallic character. The Fe-BP/Tl₂S and Tc-BP/Tl₂S are dilute magnetic semiconductors (DMSs), while TM-BP/Tl₂S (Mo-, Pd-, Ni-) systems are semiconductors. The other TM-BP/Tl₂S systems become metals. These results may open a new avenue for application of the BP/Tl₂S in future spintronic and electronic devices.

1. Introduction

At present, genuine interest is brewing in the scientific community in heterostructures that could possess the advantages of two or more two-dimensional (2D) materials and expand the functions of 2D materials. A great deal of effort has been devoted to heterostructures experimentally and theoretically, such as graphene/phosphorene,[1,2] GeSe/phosphorene,[3] phosphorene/MoS₂,[4–6] MoS₂/BN,[7–10] SiC/MoS₂,[11] graphene/bilayer-GaSe,[12] and so on.[10,13] Phosphorene, an emerging 2D material with an obvious bandgap, may be superior to the graphene for device applications in many ways and stimulates lots of theoretical research.[14–17] Of prominence, scientific progress in phosphorene-based heterostructures has been overwhelming in the fields of optoelectronics and nanoelectronics.[1,4–6,18–21] GeSe/phosphorene has an intrinsic type-II band alignment and shows great potential to act as a good candidate for applications in optoelectronics due to spontaneous electron–hole charge separation.[3]

In recent years, thallium sulfide (Tl₂S) with semiconductor properties, a representative of metal-shrouded 2D materials, has been paid more attention than other metal-shrouded 2D materials.[22–25] Moreover, the Tl₂S monolayer adopting an anti-CdCl₂ structure is theoretically verified to be thermally and dynamically stable.[26] Most importantly, the distinctive metal-shrouded structure makes monolayer Tl₂S own many intriguing properties such as strong light absorption and ideal photo-electricity transduction,[27] implying Tl₂S could be an excellent candidate for a wide range of applications in electronic and optoelectronic devices. It is interesting to explore the vdW heterostructure composed of BP and monolayer Tl₂S. Therefore, in this paper, we investigate the structural and electronic properties of BP/Tl₂S vdW heterostructures. Strain engineering is a valid way to modify the electronic and magnetic properties of 2D materials. Hence, it is significant to explore the electronic structure of the BP/Tl₂S under strains by first-principles calculations. The transitions from type-I to type-II band alignment and from semiconductor to metal are observed under uniaxial and biaxial strain.

Previous work has reported that the interlayer interaction can be effectively changed by intercalating impurity atoms between layers, leading to the electronic and magnetic properties varying accordingly. It was reported that the transition from semiconductor to metal was observed in KₓMoS₂ with increasing potassium intercalation.[28] Shahid Sattar *et al.* demonstrated that intercalating NH₃ molecules between silicene and monolayer PtSe₂ could weak the interlayer interaction.[29] Moreover, Yongji Gong *et al.* not only shown that the

aCollege of Physics and Electronics, North China University of Water Resources and Electric Power, Zhengzhou, Henan, 450046, China. E-mail: wangyusheng@ncwu.edu.cn

bCollege of Computer and Information Engineering, Henan University of Economics and Law, Zhengzhou, Henan, 450000, China

cInternational Joint Research Laboratory for Quantum Functional Materials of Henan, School of Physics and Engineering, Zhengzhou University, Zhengzhou 450001, China

dCollege of Science, Zhongyuan University of Technology, Zhengzhou 450007, China

† Electronic supplementary information (ESI) available. See DOI: 10.1039/c9ra03547h

intercalation method was workable, but also found that the TM was advantageous over alkali metals, rare earth metals when they were intercalated crystals.[30] Lately, a new study found that the bilayer WSe_2 intercalated with TMs (Cr, Mn, Fe, Co, Ni) exhibited a half-metallic character with a 100% spin polarization at the Fermi level due to the strong hybridization between the TMs and the parent W and Se atoms.[31] These inspire us to study the structural, electronic and magnetic properties of the BP/Tl_2S intercalated with all kinds of TMs (3d and 4d TM atoms). The results indicated that the half-metal and DMS character were induced in the BP/Tl_2S by intercalating TMs. These findings may provide a new route for looking for the suitable candidate materials for spintronic devices, owing to the half-metallic and DMS properties of the BP/Tl_2S intercalated with TMs (V, Cr, Mn, Fe, Tc).

2. Computational details

The present calculations are performed by employing spin-polarized density functional theory as implemented in the Vienna Ab initio Simulation Package (VASP).[32–34] We adopt the optB88-vdW[35,36] density functional to describe the long range vdW interaction because it can give a reasonable description for various layered compounds systems such as $tellurene/MoS_2$ heterostructure,[37] chromium trihalide[38] and so on. The exchange and correlation functional is treated using the generalized gradient approximation (GGA) in the Perdew–Burke–Ernzerhof (PBE).[39] A kinetic energy cutoff 500 eV is used in all simulations. An enough large vacuum layer thickness of 20 Å is added to each heterostructure to avoid spurious interaction between periodic images in the out-of-plane direction. The first Brillouin zone is sampled with a $7 \times 5 \times 1$ Monkhorst–Pack grid for the relaxation of BP, Tl_2S, BP/Tl_2S and the TM-BP/Tl_2S, respectively. All the structures are fully relaxed with an energy and a force tolerance of 10^{-5} eV and 0.01 eV $Å^{-1}$ respectively.

3. Results and discussion

3.1 BP/Tl_2S

In view of the optimized structure, the optimized lattice constants of BP in our calculation are $a = 3.297$ Å and $b = 4.615$ Å, which are in good agreement with the previous results.[40,41] Our optimized lattice constant for Tl_2S is $a_1 = a_2 = 4.18$ Å, which also agrees with the cell parameters of the single crystal reported by the experiment.[42] Using a lattice match model, the combination of a 2×2 periodicity of BP ($a = 6.59$ Å, $b = 9.22$ Å, containing 16 P atoms) and a Tl_2S monolayer supercell ($b_1 = \sqrt{3}a_1 = 7.24$ Å, $b_2 = 2a_2 = 8.37$ Å, containing 4 S and 8 Tl atoms) is used for the simulation of the BP/Tl_2S vdW heterostructure. In order to decrease the lattice mismatch between BP and Tl_2S, the lattice constant is compressed or stretched to be $a = 6.80$ Å and $b = 8.88$ Å in the BP and Tl_2S supercell, leading to a lattice mismatch of around 6.08%, 6.01% in both (x and y) directions. There are no significant changes of the electronic structure observed in BP and Tl_2S because the sublattice

symmetry is still maintained. Therefore, the BP/Tl_2S is expected feasible in theory.

According to the geometry properties of the monolayer BP and Tl_2S, for simplicity sake, only two representative configurations are taken into account, namely, A-stacking and B-stacking. The corresponding fully optimized top and side view of the BP/Tl_2S are shown in Fig. 1(c) and (d). As for A-stacking, the half Tl atoms of the bottom layer of Tl_2S marked by the red dashed circle are placed above the P atoms of the top layer of BP, whereas another half Tl atoms marked by the blue dashed circle are located above the puckered hexagon center of BP (see in Fig. 1(c)). For B-stacking, all the lower Tl atoms labeled by the yellow dashed circle are placed on top of bridge site (see Fig. 1(d)). In order to find essentially the most stable stacking manner, the binding energy (E_b) between the stacking layers in the BP/Tl_2S is calculated as follows:

$$E_b = [E(BP/Tl_2S) - E(BP) - E(Tl_2S)]/n \tag{1}$$

where $E(BP/Tl_2S)$ is the total energy of the BP/Tl_2S, and $E(BP)$, $E(Tl_2S)$ are the energies of the isolated BP monolayer and Tl_2S monolayer respectively. n is the total number of the P atoms in a 2×2 supercell. According to this definition, the positive value of E_b corresponds that the interaction is exothermic and hence stable. Moreover, a more positive binding energy indicates a stronger binding between the BP and Tl_2S. The binding energies for A-stacking and B-stacking are 748.50 meV, 750.04 meV, respectively. One can find that B-stacking is the energetically favorable pattern with the higher binding energy and the shorter interlayer distance. The difference of E_b between A- and B-stacking is extraordinarily small (about 1.5 meV), which suggests that the stacking pattern doesn't show a significant influence on the total energy of the heterostructure. Even so, for the sake of convenience for research, we choose the energy-lowest B-stacking to represent the most stable configuration as a further research in this paper. Moreover, the total energy varies with the variation of the interlayer distance of the B-stacking heterostructure is shown in Fig. S1.† It is found that the value of interlayer distance is about 3.35 Å.

To further clarify the interaction between BP and Tl_2S, the charge density difference $\Delta\rho(z)$ along the z direction is calculated by using the following equation:

$$\Delta\rho(z) = \rho(BP/Tl_2S) - \rho(BP) - \rho(Tl_2S) \tag{2}$$

where $\rho(BP/Tl_2S)$, $\rho(Tl_2S)$, $\rho(BP)$ are the charge densities of the BP/Tl_2S, the isolated Tl_2S and the BP monolayer, respectively. In addition, the amount of transferred charge along the z direction is defined as follows:

$$\Delta Q(z) = \int_{-\infty}^{z} \Delta\rho(z')dz' \tag{3}$$

The vivid differential charge density of BP/Tl_2S is shown in the inset of Fig. 2(a). The yellow and blue colors indicate the charge accumulation and depletion of the BP/Tl_2S. One can see clearly from Fig. 2(a) that BP donates electrons to the Tl_2S layer,
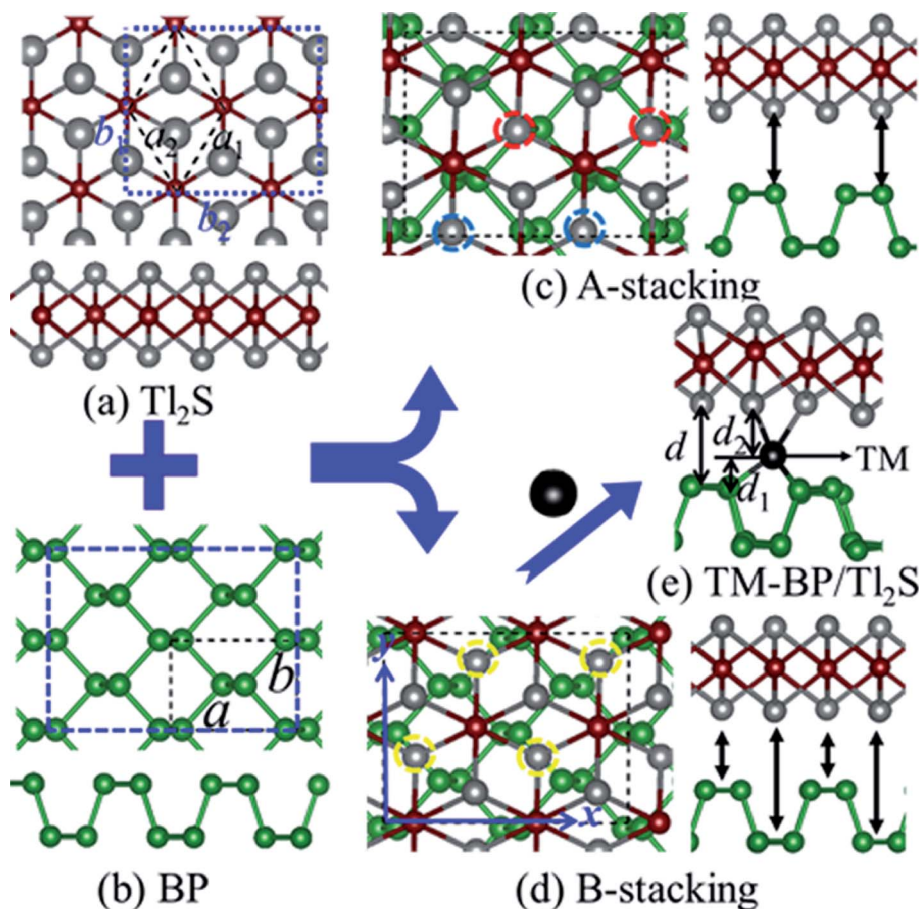
Fig. 1   The top and side view of (a) Tl_2S, (b) BP. (c) A-stacking of the BP/Tl_2S, (d) B-stacking of the BP/Tl_2S. (e) The BP/Tl_2S heterostructure with TM atoms intercalated. The green, gray, wine red and black balls represent P, Tl, S and TM atoms, respectively.

which leads to p-doping in BP layer. In addition, in order to explore its interlayer properties, the plane-averaged electrostatic potential along the perpendicular direction (z direction) of the BP/Tl_2S is shown in Fig. 2(b). The striking characteristics is that there exists a large potential drop of ΔV across the BP/Tl_2S interface 9.91 eV, which is much larger than the values of the GeSe/BP (5.94 eV),[3] graphene/BP (6.42 eV),[19] blue phosphorene/ g-GaN (7.31 eV) and blue phosphorene/graphene (5.84 eV).[43]

Such a large potential drop implies that there exists a strong electrostatic field between BP and Tl_2S, which is in favors of charge injection, leading to the better device performance if the BP/Tl_2S is put into practical use.

It is also necessary to analyze the band structure of the BP/ Tl_2S, in order to comprehensively understand the properties of the BP/Tl_2S. The separate BP monolayer and Tl_2S are direct band gap semiconductors with the valence band maximum
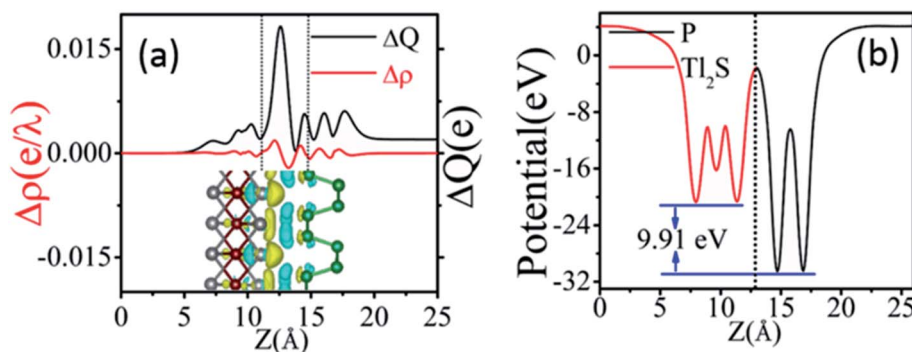

Fig. 2   (a) The planar-averaged differential charge density of the BP/Tl_2S heterostructure ($\Delta\rho(z)$), and the amount of transferred charge along the z direction ($\Delta Q(z)$). (b) The planar-averaged electrostatic potentials of the BP/Tl_2S heterostructure. The inset in (a) shows charge density difference with an isovalue of 0.0025 e Å^{-3}. The yellow and blue regions denote the gain and loss of electrons, respectively.

(VBM) and the conduction band minimum (CBM) at the Γ point (see Fig. 3(a) and (b)), the corresponding bandgaps are 0.894 eV and 1.37 eV, respectively, which are in agreement with the previous theoretical calculations.[26] However, the BP/Tl$_2$S becomes an indirect bandgap semiconductor with the VBM at the A point and CBM at the Γ point (see Fig. 3(c)). The bandgap of the BP/Tl$_2$S is 0.79 eV. The partial charge densities of the BP/Tl$_2$S for CBM and VBM are depicted in Fig. 3(d) and (e). It is clearly showed that the CBM is dominated by S atoms and the VBM comes mainly from S and Tl atoms. Hence, the type-I band alignment is obtained due to CBM and VBM being from the Tl$_2$S in the BP/Tl$_2$S, which is accord with the band structure of BP/Tl$_2$S (Fig. 3(c)). In order to find out the effect of stacking type on the band structure, we also calculated the band structure of A stacking BP/Tl$_2$S as shown in Fig. S4.† It can be found that the band structures of the two stacking types are almost the same. The band gaps are 0.796 eV and 0.794 eV for A-stacking and B-stacking, respectively. The tiny difference of band gap indicates that the stacking type of BP/Tl$_2$S has little influence on the band structure of BP/Tl$_2$S.

To examine the effect of spin–orbital-coupling (SOC)[44] on the band structure of BP/Tl$_2$S, we calculated the band structure of the heterostructure by considering SOC effect (Fig. S2†). There is no obvious difference in the band structures of BP/Tl$_2$S with and without SOC effect, suggesting that the SOC effect is negligible.

The carrier mobility of the heterostructure has a great effect on the performance of electronic devices.[45] Therefore, according to the following formula, we calculate the effective mass of holes and electrons of BP/Tl$_2$S

$$m^* = \hbar^2 \left(\frac{\partial^2 E}{\partial k^2} \right)^{-1} \qquad (4)$$

where $\hbar$ is Planck's constant and k is the wave vector in momentum space. The effective masses in BP/Tl$_2$S are 0.21 m_e alone the x direction (0.85 m_e alone the y direction) for holes and 1.35 m_e alone the x direction (6.23 m_e alone the y direction) for electrons, which are larger than those in graphene and BP.[46,47]

The application of strain has been proved to be a very effective approach to modulate the electronic properties of 2D materials. Very recently, Peng *et al.* revealed that the band structure of BP can be effectively tuned *via* the application of axial strain.[48] Thus, we believe that a controllable band gap of the BP/Tl$_2$S may also be obtained by this approach. By calculating the band gaps of BP/Tl$_2$S at different values of axial strains, we find that the strain has a remarkable effect on the band structures (see Fig. 4). We can see the same characters that the band gap monotonically decreases with an increase of tensile and stress strain in the x and y direction and biaxial uniform strain. For the strain applied in the biaxial uniform situation, the gap sharply drops to 0 eV from the initial value of 0.79 eV at −6% and +7% (see Fig. 5(a) and (j)). For the strain
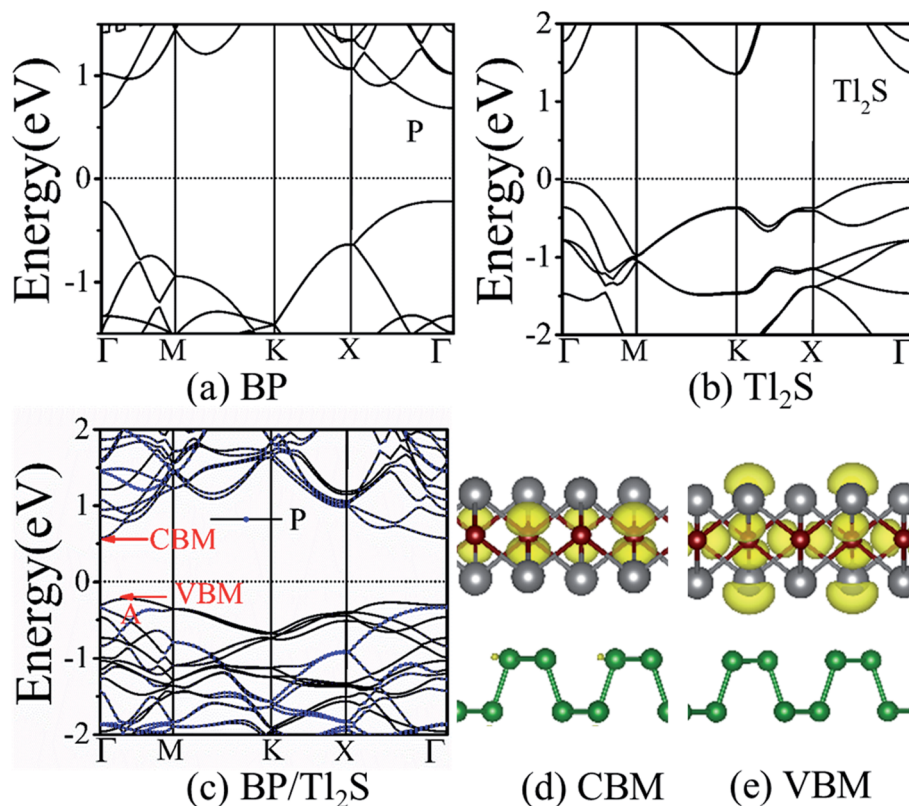

Fig. 3 Band structures for (a) the monolayer BP, (b) the monolayer Tl$_2$S, (c) the BP/Tl$_2$S heterostructure. The band partial charge density of the BP/Tl$_2$S heterostructure: (d) CBM, (e) VBM. The value of isosurfaces is 0.0025 e Å^{-3}.
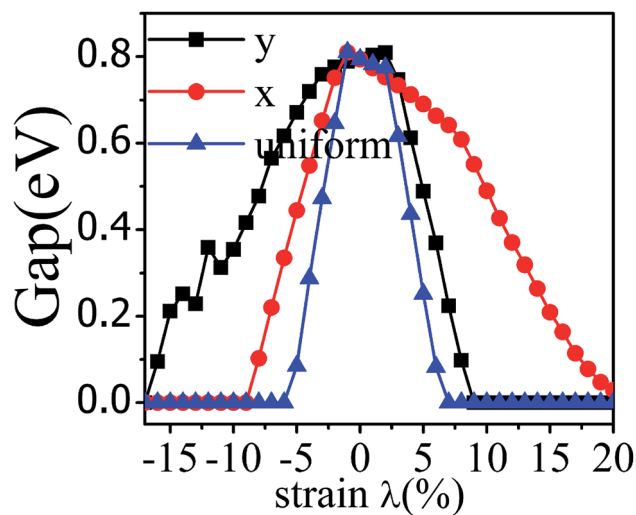
Fig. 4 The band gap of the BP/Tl$_2$S as a function of strain (λ%) applied in x, y direction and biaxial uniform strain.

applied in x direction, the band gap is sensitive to stress strain and decrease to zero at −8% (see Fig. 6(a)). However, the gap decreases tardily to 0.49 eV at +10% tensile strain. In order to see if the gap can reduce to zero with further increased tensile strain, we explore even larger strain up to +25% with a 1% increment. We find the band gap reaches a minimal value of 0.011 eV at +22% and then opens up again for larger strain (see Fig. 6). On the contrary, for the strain applied in y direction, the band gap is more sensitive to tensile strain than stress strain. The band gap becomes to zero at +9% (see Fig. 7(l)), while the

band gap does not become zero until the stress strain increases to −17% (see Fig. 7(f)).

In addition, we find an interesting semiconductor–metal and indirect–direct transition of energy gap under suitable strain. In detail, for the strain applied in the biaxial uniform situation in Fig. 5, the VBM moves from A point to Γ point gradually with an increase of tensile strain, while the CBM keeps at Γ point. Hence, the band gap undergoes indirect–direct transition under +6% tensile strain (see Fig. 5(i)). The CBM moves down and goes through the Fermi level at +7% tensile strain (see Fig. 5(j)), resulting the metal character. In the case of stress strain, the gap maintains indirect all through. The indirect band gap converts to zero at −6% stress strain (see Fig. 5(a)), making the BP/Tl$_2$S becoming metal. Interestingly, the CBM is contributed by BP, while the VBM is contributed by Tl$_2$S under tensile strain. Inversely, the CBM is mainly from Tl$_2$S and the VBM is entirely from the BP under the stress strain. Hence, the CBM and VBM of the BP/Tl$_2$S are provided by two different materials in the biaxial uniform situation, which implies a distinct type-II band alignment. For the strain applied in the x direction, the band gap is indirect with the VBM at A point and CBM at Γ point under stress strain of −8% to 0% (see Fig. 6). Once the stress strain exceeds −8%, the band gap changes to zero, inducing that the BP/Tl$_2$S becomes metal. In the case of tensile strain, the band gap is still indirect with the VBM at A point, while the CBM shifted from Γ to A under stress strain above +8%, indicating an indirect-to-direct gap transition at +8% (see Fig. 6(i)). Interestingly, the CBM and VBM simultaneously move in the opposite direction, namely, shift from A point to Γ point little by little in the range of +8% to +14%. Hence, the band gap is direct with the CBM and VBM at Γ point under stress strain above +14%.
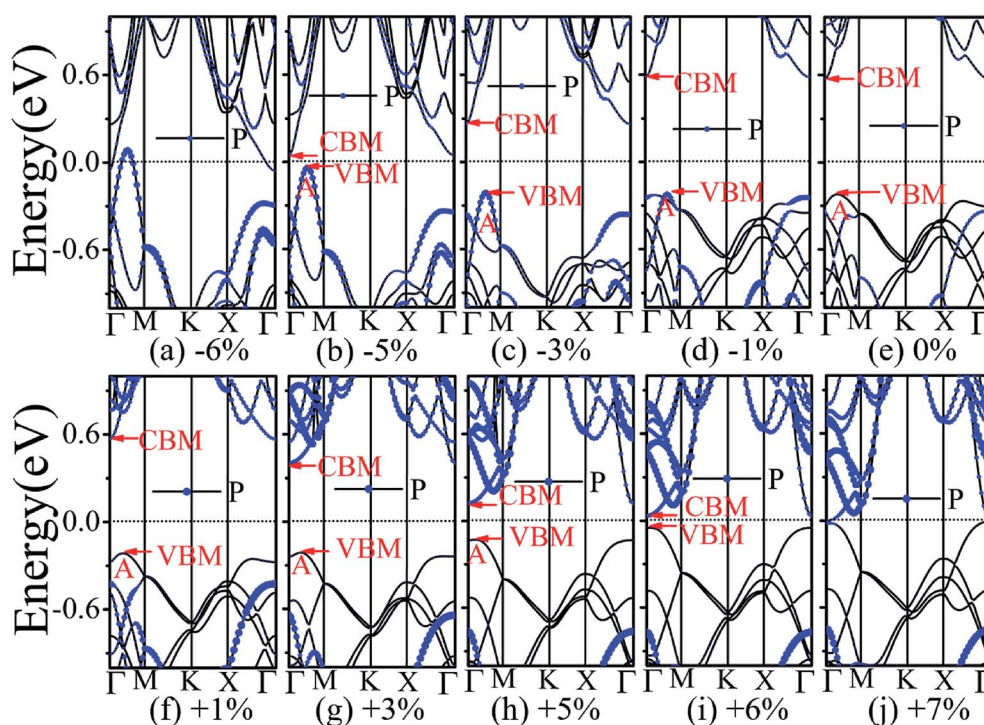

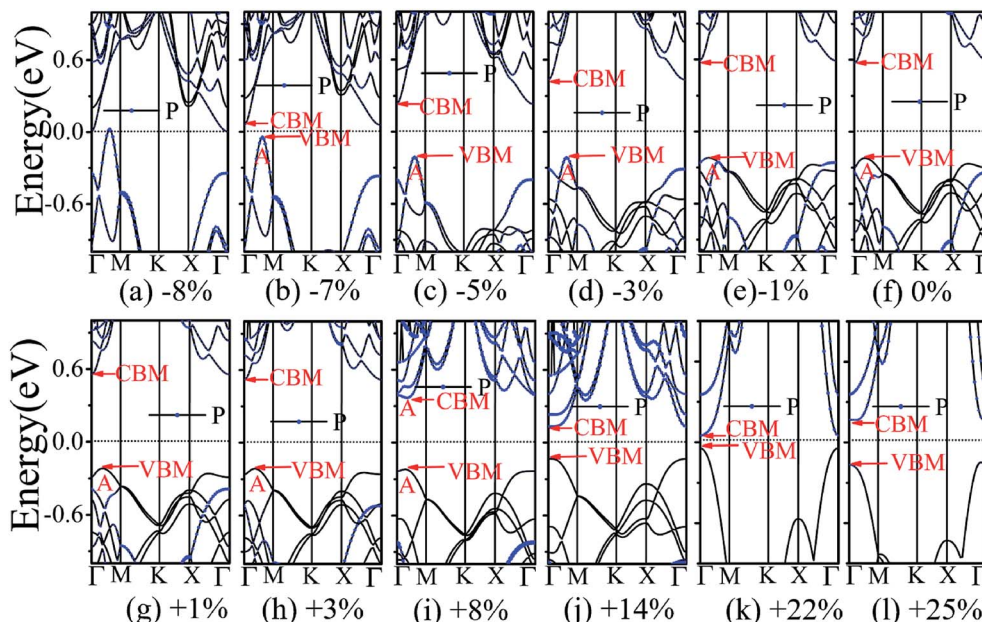**Fig. 5** The band structures of the BP/Tl$_2$S with different biaxial uniform strain.

Fig. 6 The band structures of the BP/Tl$_2$S with different strain along the *x* direction strain.

The band gap downgrades to minimum (0.011 eV) at +22%, then increases rapidly almost tenfold (0.11 eV) at +25% (see Fig. 6(k) and (l)).

Surprisingly, there also exists the band arrangement transition. The BP/Tl$_2$S is still type-I under −1% to +3%, due to both the CBM and VBM of the BP/Tl$_2$S lying in absolutely Tl$_2$S. Furthermore, with further increase of the strain, the BP/Tl$_2$S becomes type-II semiconductor, because the VBM are from the BP, and the CBM comes from Tl$_2$S under the stress strain below −3%, while the source of CBM and VBM appears opposite

phenomenon under stress strain above +8%, which can be clearly seen in Fig. 6(i)–(l). For the strain applied in the *y* direction, with an increase of stress strain, the energy of Γ point is higher than that of A point at −3% (see Fig. 7(e)), indicating an indirect-to-direct gap transition. Then the band gap transitions back to indirect at −6% (see Fig. 7(d)). The band gap becomes zero at −17% (see Fig. 7(a)), and the BP/Tl$_2$S turns into metal. On the side of tensile strain, the VBM is always located at A point, however, the CBM undergoes an interesting transition from Γ to B at +7% (see Fig. 7(j)). Therefore, the band gap
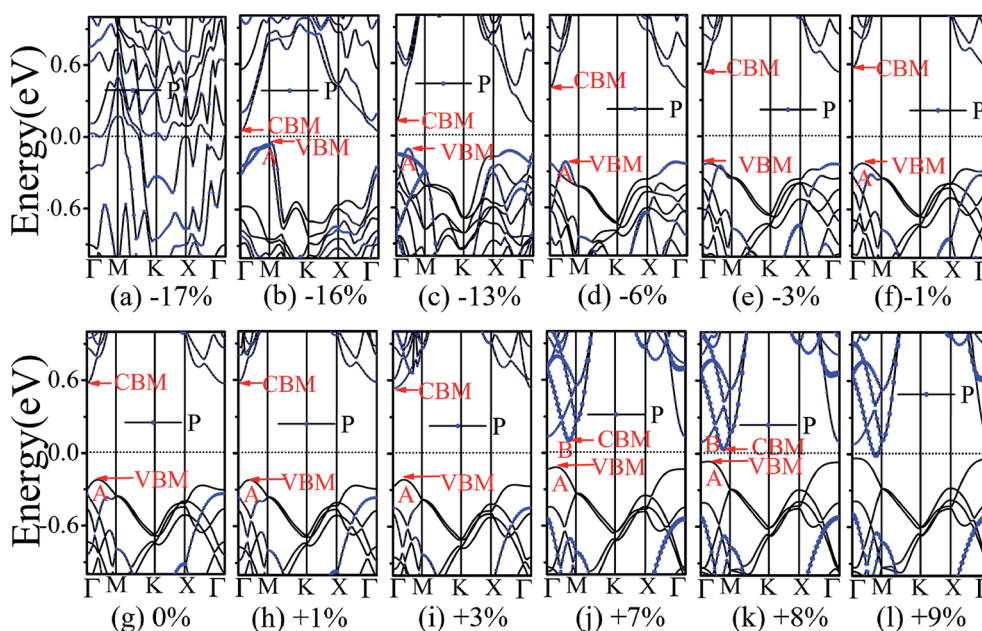

Fig. 7 The band structures of the BP/Tl$_2$S with different strain along the *y* direction.

remains indirect under tensile strain. It is clear that the BP/Tl_2S displays the metallic feature due to the CBM moving down and crossing the Fermi level at +9% (see Fig. 7(l)). What's more, we also find meaningfully the band arrangement transition. For example, both the CBM and VBM of BP/Tl_2S are completely localized on Tl_2S under −3% to +3% (see Fig. 7(e)–(i)), which emerges a natural type-I band arrangement. Furthermore, with the further increase of strain, the type-I heterostructure transforms to type-II because the VBM and CBM are from the both different material of the BP/Tl_2S, which can be carefully confirmed in Fig. 6.

3.2 BP/Tl_2S with TM atoms intercalated

From a technical point of view, defects,[49,50] adatom adsorption,[51–53] and chemical decorations[54,55] are all fundamentally and widely employed techniques for tuning the electronic and magnetic properties of 2D materials. Recently, it is reported that intercalating impurity atoms between layers of heterostructures also is an effective strategy to drive magnetism.[56] Therefore, we focus on intercalating TMs (3d and 4d) in the BP/Tl_2S (TM-BP/Tl_2S) to investigate their electronic and magnetic properties. Firstly, we determine the most stable position of the 3d TMs in BP as well as 4d TMs. By comparing adsorption energies of 4d TMs on the three possible adsorption sites (on top of P (T), on top of the hexagonal hollow site (H) and on top of the bridge site of P–P bond (B)), it is found that the H site is the preferable adsorption site with the lowest binding energies (3.47 eV, 5.98 eV, 4.14 eV, 3.15 eV, 4.32 eV, 5.08 eV, 4.95 eV, 3.42 eV, 1.12 eV, 0.13 eV for Y to Cd, respectively). As for 3d TMs, Kulish *et al.* have performed a systematic study on the binding energy, geometry, and electronic structure of BP with adsorption of 3d TMs.[57] The results show that the H site is also energetically favors due to the adsorption energies being the largest for all the TMs.

Then, we place the monolayer Tl_2S on top of the BP with one TM adsorbed (Fig. 1(e)). In order to search for the favorable intercalating position and optimize the interlayer distance (*d*) of TM-BP/Tl_2S, we employ the following method: we investigate the optimal relative in-plane position by shifting the Tl_2S layer at first with a fixed layer distance, at the same time, TM is allowed to move freely between layers, and then we relax and optimize the layer distance with the optimized relative in-plane position. To theoretically estimate the structural stability of the TM-BP/Tl_2S systems, the binding energies (E_{bTM}) of TM in TM-BP/Tl_2S systems are calculated using the following formula:

$$E_{bTM} = E(TM\text{-}BP/Tl_2S) − E(BP) − E(Tl_2S) − E(TM) \quad (5)$$

where $E(TM\text{-}BP/Tl_2S)$ is the total energy of the TM-BP/Tl_2S system, $E(BP)$ and $E(Tl_2S)$ are the energy of the BP monolayer and the Tl_2S monolayer, respectively. $E(TM)$ is the energy of an isolated TM atom. A summary of the obtained results is listed in Table 1. The binding energies of TMs in the TM-BP/Tl_2S systems are larger than the values of TMs adsorbed on BP, indicating that the BP/Tl_2S intercalated with TMs is more stable than TM adsorbed on the BP. It is worth mentioning that the binding energies of Zn and Cd are 0.28 eV and 0.29 eV, respectively,

which are much less than the corresponding cohesive energies of TMs (1.35 eV, 2.95 eV), suggesting Zn and Cd tend to form clusters rather than distribute evenly when intercalated in BP/Tl_2S. Therefore, we would not discuss Zn-BP/Tl_2S and Cd-BP/Tl_2S systems in the following sections. Interestingly, we find the binding energies of 4d TMs are larger than the values of homdogy 3d TMs in the periodic table. In addition, after full relaxation, it is found that the most TMs (Sc to Cu for 3d TM, Y to Pd for 4d TM) still prefer to adsorb at the H site of BP. However, the Ag atom is preferable to the T site. It can be seen from Table 1 that the TMs exert significant influence on the interlayer distance. The most interlayer distance (*d*) of the TM-BP/Tl_2S is larger than that of the BP/Tl_2S. The interlayer distance of a few TM-BP/Tl_2S systems (Sc-, Fe-, Co-, Y-, Nb-, Pd-BP/Tl_2S) are smaller than that of the BP/Tl_2S. The V-BP/Tl_2S system is exception, in which the interlayer distance is found to be fully equal to that of the BP/Tl_2S. Typically, almost all TMs are closer to the BP layer, except that Y is closer to Tl_2S, due to Y being bonded to S atom.

It is well known that d-shell electrons of TMs are localized and unstable, which may cause rearrangement of substrate electrons when TMs are adsorbed. Therefore, it is necessary to perform the Bader charge analysis[58] to determine the transferred charges between the TMs and BP/Tl_2S. The results show that intercalating TMs has a very important impact on the charge redistribution of the BP/Tl_2S. As for 3d and 4d TMs, there exists the same following phenomenon in the charge transfer: most of the TMs lose electrons, and the lost charges gradually decrease as the atomic number increases. Specifically, the Co of 3d TM and the Ru, Rh, Pd of 4d obtain charges from the BP/Tl_2S (see Table 1). Accordingly, the electrons obtained by BP decrease basically as the atomic number increases from Sc to Ni for 3d TMs (from Y to Ru for 4d TMs). On the contrary, the donated charges by Tl_2S increase basically as the atomic number decreases from V to Ni for 3d TMs (from Nb to Pd for 4d TMs). In all TM-BP/Tl_2S systems, only the BP layer of Rh-BP/Tl_2S system donates a few charges to Rh, leading to p-doping effect on the BP. As for Sc-, Ti-, Y- and Zr-BP/Tl_2S systems, TMs transfer charges to BP/Tl_2S, which leading to n-doping in the BP/Tl_2S.

In order to explore the possible application prospects of the various TM-BP/Tl_2S systems, it is quite necessary to study the electronic and magnetic properties of the various TM-BP/Tl_2S systems. As shown in Table 2, the most TM-BP/Tl_2S (Sc-, Co-, Ni-, Cu-, Y-, Zr-, Nb-, Mo-, Ru-, Rh-, Pd-, Ag-) systems have the ground states with non-spin polarization, while the monolayer BP adsorbed by Sc, Co, Y, Nb, Ru are spin polarized, which indicate that the Tl_2S has significant influence on the electronic properties of TM-BP. We notice that the TM-BP/Tl_2S (Ti-, V-, Cr-, Mn-, Fe-, Tc-) systems are similar to TM-BP (Ti-, V-, Cr-, Mn-, Fe-, Tc-), possess the spin polarized ground states. Nevertheless, compared with the corresponding magnetic moment values of TM-BP (Ti-, V-, Cr-, Mn-, Fe-, Tc-),[57] the magnetic moments of the TM-BP/Tl_2S (Ti-, V-, Cr-, Mn-, Fe-, Tc-) systems vary from 0.570 μ_B to 3.406 μ_B, which are significantly reduced, owing to the interaction between TMs and BP/Tl_2S being stronger than the interaction between TMs and BP, which is verified by the

Table 1 The binding energies (E_b and E_{bTM}) of the TM atoms adsorbed on the monolayer BP and intercalated in the BP/Tl$_2$S heterostructure, the TM−P bond length ($d_{TM−P}$), the TM−Tl bond length ($d_{TM−P}$), the distances between TM and the upper layer P atom of BP (d_1), the distances between TM and the lower layer Tl atom of Tl$_2$S (d_2), the interlayer distance (d), the most favorable intercalating sites, the transfer charges (Q) and the band gap are listed respectively. The TM atoms, BP and Tl$_2$S transfer electronic charges obtained using Bader charge analysis (labeled Q_{TM}, Q_P, Q_{Tl2S}, respectively). The negative and positive Q represent the loss and gain of electrons, respectively. E_b of 3d TMs (Ti–Cu) adsorbed on BP comes from ref. 51

	E_{bTM} (eV)	E_b (eV)	$d_{TM−Tl}$ (Å)	$d_{TM−P}$ (Å)	d_1 (Å)	d_2 (Å)	d (Å)	Q_{TM} (e)	Q_P (e)	Q_{Tl2S} (e)	E_{gap} (eV)
Sc	4.32	3.43	2.98	2.55	1.74	1.39	3.12	−1.344	1.098	0.246	0(M)
Ti	6.11	3.41	2.86	2.51	1.52	2.03	3.56	−1.089	1.013	0.076	0(M)
V	4.31	2.68	2.79	2.44	1.41	1.94	3.35	−0.835	0.886	−0.051	0(H)
Cr	2.71	1.66	2.68	2.51	1.44	2.15	3.59	−0.640	0.713	−0.073	0(H)
Mn	3.05	1.78	2.6	2.40	1.22	2.19	3.41	−0.463	0.617	−0.154	0(H)
Fe	4.76	2.70	2.77	2.41	1.20	2.02	3.22	−0.224	0.436	−0.212	0.42(I)
Co	5.42	3.56	2.55	2.15	0.85	2.40	3.25	0.010	0.246	−0.256	0(M)
Ni	5.49	4.09	2.55	2.38	1.18	2.30	3.47	−0.014	0.248	−0.234	0.67(I)
Cu	3.03	2.18	2.57	2.31	1.20	2.24	3.44	−0.189	0.382	−0.194	0(M)
Y	5.24	3.47	3.29	2.82	2.06	1.18	3.24	−1.548	1.001	0.547	0(M)
Zr	6.02	5.98	3.02	2.51	1.54	1.93	3.47	−1.199	1.043	0.156	0(M)
Nb	6.16	4.14	2.97	2.48	1.24	2.03	3.27	−0.919	1.016	−0.097	0(M)
Mo	5.28	3.35	2.88	2.34	1.49	1.88	3.37	−0.428	0.587	−0.159	0.42(I)
Tc	6.27	4.32	2.79	2.27	1.47	2.08	3.55	−0.093	0.330	−0.237	0.13(I)
Ru	6.55	5.08	2.22	3.20	1.22	2.24	3.46	0.184	0.053	−0.237	0(M)
Rh	6.24	4.95	3.45	2.26	1.29	2.26	3.55	0.278	−0.02	−0.258	0(M)
Pd	4.36	3.42	3.46	2.39	1.23	2.08	3.31	0.205	0.048	−0.253	0.74(I)
Ag	1.48	1.12	2.85	2.76	2.40	1.34	3.73	−0.079	0.261	−0.182	0(M)

Table 2 Total magnetic moment (M_{total}), magnetic moment of the TM atoms intercalated (M_{TM}), the BP/Tl$_2$S (M_p and M_{Tl2S}) of the six magnetic TM-BP/Tl$_2$S systems

	M_{tot} (μ_B)	M_{TM} (μ_B)	M_P (μ_B)	M_{Tl2S} (μ_B)
Sc	0	0	0	0
Ti	0.894	0.795	0.072	0.028
V	0.872	0.902	−0.038	0.007
Cr	3.406	3.356	0.003	0.047
Mn	2.679	2.644	−0.017	0.052
Fe	1.788	1.657	0.021	0.109
Co, Ni, Cu	0	0	0	0
Y, Zr, Nb, Mo	0	0	0	0
Tc	0.570	0.391	0.116	0.062
Ru, Rh, Pd, Ag	0	0	0	0

The distinguishing feature of the magnetic moment contribution is that the magnetic moments are mainly localized on the interlayer TMs for the TM-BP/Tl$_2$S (Ti-, V-, Cr-, Mn-, Fe-, Tc-), and a tiny amount of the magnetic moments are induced by the adjacent P and Tl atoms, which is similar to the above results in Table 2. There exists the same phenomenon of magnetic moment distribution in other systems, such as TM-Tl$_2$S systems,[26] TM@(graphene/MS$_2$)[56] and so on.

To illustrate the magnetic moment origin of the TM-BP/Tl$_2$S (Ti-, V-, Cr-, Mn-, Fe-, Tc-), we calculate the total density of states (TDOS) and projected density of states (PDOS) of the TMs and its nearest P, Tl and S atoms, as is represented in Fig. 9. It is seen that the TM (Ti, V, Cr, Mn, Fe, Tc) atomic states are dominant near the Fermi level, while few atomic states are from the nearest P, Tl and S atoms, indicating that magnetic moments of these systems (Ti-, V-, Cr-, Mn-, Fe- and Tc-BP/Tl$_2$S) are mainly contributed by the TM d orbital. Moreover, the hybridization between the TM d orbitals and p or s orbitals of the nearest P, Tl atoms occurs in the energy range of −0.9 eV to 0.25 eV, due to energy peaks at the same energy, which results in the splitting of the energy levels near the Fermi level and are
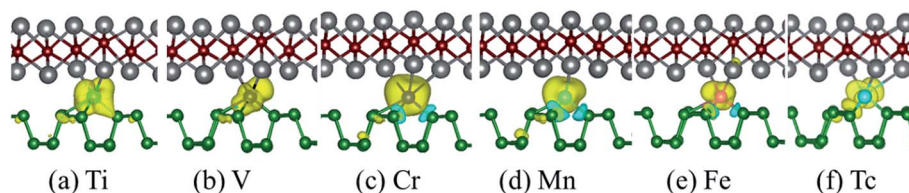
binding energies discussed in Table 1. In addition, it can be seen from Table 2 that the total magnetic moments mainly come from TMs. Furthermore, in order to visualize the magnetic moment distribution of the TM-BP/Tl$_2$S (Ti-, V-, Cr-, Mn-, Fe-, Tc-), we display the spin density distributions in Fig. 8.

(a) Ti   (b) V   (c) Cr   (d) Mn   (e) Fe   (f) Tc

Fig. 8 Spin density (up−down) with an isovalue of 0.0025 e Å^{-3} for six magnetic TM-BP/Tl$_2$S systems: (a) Ti-BP/Tl$_2$S, (b) V-BP/Tl$_2$S, (c) Cr-BP/Tl$_2$S, (d) Mn-BP/Tl$_2$S, (e) Fe-BP/Tl$_2$S, (f) Tc-BP/Tl$_2$S. Yellow and blue indicate the spin up and spin down densities, respectively.
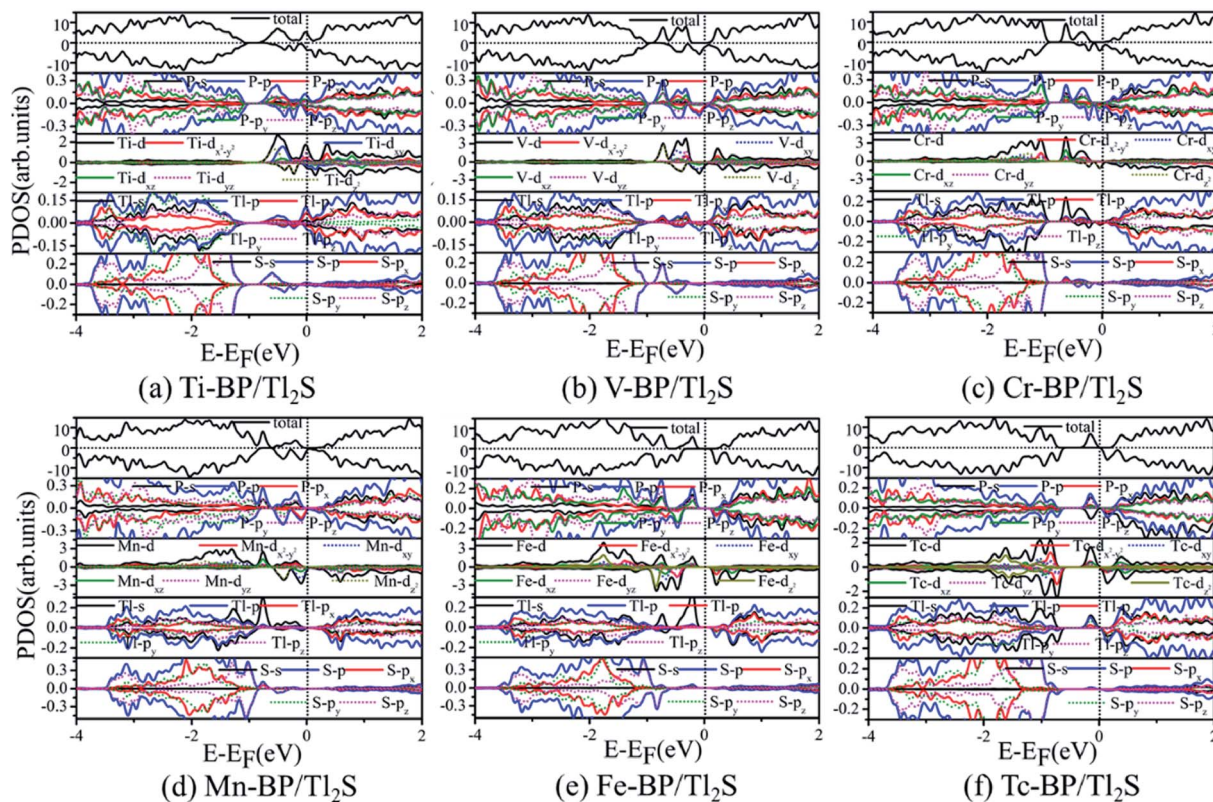
Fig. 9 PDOS for six magnetic TM-BP/Tl$_2$S systems: (a) Ti-BP/Tl$_2$S, (b) V-BP/Tl$_2$S, (c) Cr-BP/Tl$_2$S, (d) Mn-BP/Tl$_2$S, (e) Fe-BP/Tl$_2$S, (f) Tc-BP/Tl$_2$S.

responsible for the magnetic moments. Furthermore, the magnetic moments obviously depend on different d orbitals. For Ti-BP/Tl$_2$S system, the Ti-d_{xy} and -d_{z^2} orbitals and the degenerate p_x, p_y and p_z orbitals of P, p_x orbitals of Tl hybridize and split at Fermi level, which caused the distinct magnetic moments. For V-, Cr- and Mn-BP/Tl$_2$S systems, they share the similar characteristics that the spin up atomic states have a clear gap while the spin down atomic states occupy the Fermi level, suggesting the half-metallic feature, which agrees with the results of the band structures giving below. However, the magnetic moments are from the different d orbitals, which are d_{yz}, d_{xy}, d_{z^2} of the V atom, d_{z^2}, d_{xz} of the Cr atom and d_{xy}, d_{z^2} of Mn atom respectively. For Fe-BP/Tl$_2$S, there exists complicated phenomenon because Fe atom has more than 5 electrons of 3d orbital and some of the nonbonding orbitals are filled. The Fe d_{yz}, d_{xz} orbitals and the degenerate p_y, p_z and s orbitals of P, s orbitals of Tl hybridize and split below Fermi level, while the Fe $d_{x^2-y^2}$ orbital and p_x, s orbitals of P, the degenerate p_y, p_x orbitals of Tl hybridize and split above Fermi level. Hence, Fe d_{yz}, d_{xz} and $d_{x^2-y^2}$ orbitals mainly contribute to the magnetic moments near the Fermi level. For Tc-BP/Tl$_2$S system, the degenerate $d_{x^2-y^2}$, d_{xz} and d_{yz} not only are asymmetrically localized at the Fermi level, but also hybridize with s and p of P and Tl, inducing the magnetic moments. Based on the above analysis of TDOS and PDOS, it is easy to reach the conclusion that the magnetic moments are mainly localized on the TMs, which is agreement with the spin density distribution plotted in Fig. 9.

Next, we turn to discuss the band structure properties of the various TM-BP/Tl$_2$S systems. We also test the SOC effect on their band structures. Take Ni-BP/Tl$_2$S as an example, the band structures with and without SOC are almost the same (Fig. S3†). So that, the SOC effect is also negligible in TM-BP/Tl$_2$S systems. As mentioned before, the TM-BP/Tl$_2$S (Y-, Zr-, Nb-, Mo-, Ru-, Rh-, Pd-, Ag-, Sc-, Co-, Ni-, Cu-) systems are nonmagnetic since the two spin states match each other (see Fig. 10(a)–(l)). It can be clearly seen from Fig. 10 that the nonmagnetic TM-BP/Tl$_2$S (Y-, Zr-, Nb-, Ru-, Rh-, Ag-, Sc-, Co-, Cu-) systems possess metallic character, because the interaction between TMs and BP/Tl$_2$S make part of energy bands go through the Fermi level. The Ni-, Mo- and Pd-BP/Tl$_2$S systems have no magnetism and still maintain semiconducting features. The indirect band gaps of the Ni-, Mo- and Pd-BP/Tl$_2$S systems are 0.67 eV, 0.43 eV, 0.74 eV, respectively, which are lower than that of the BP/Tl$_2$S. However, the magnetic V-, Cr- and Mn-BP/Tl$_2$S systems have lost their semiconducting nature, and display half-metallic character, because the up and down spin states obviously split and the spin up states maintain semiconducting feature with a narrow band gap, while the spin down states show metallic feature (see Fig. 10(n)–(p)). Moreover, the Tc- and Fe-BP/Tl$_2$S systems show a magnetic semiconducting nature with an indirect band gap (0.13 eV and 0.42 eV), indicating DMS can be obtained by intercalating Tc and Fe in BP/Tl$_2$S, which provide a new route for the potential applications of DMS in spintronic devices.
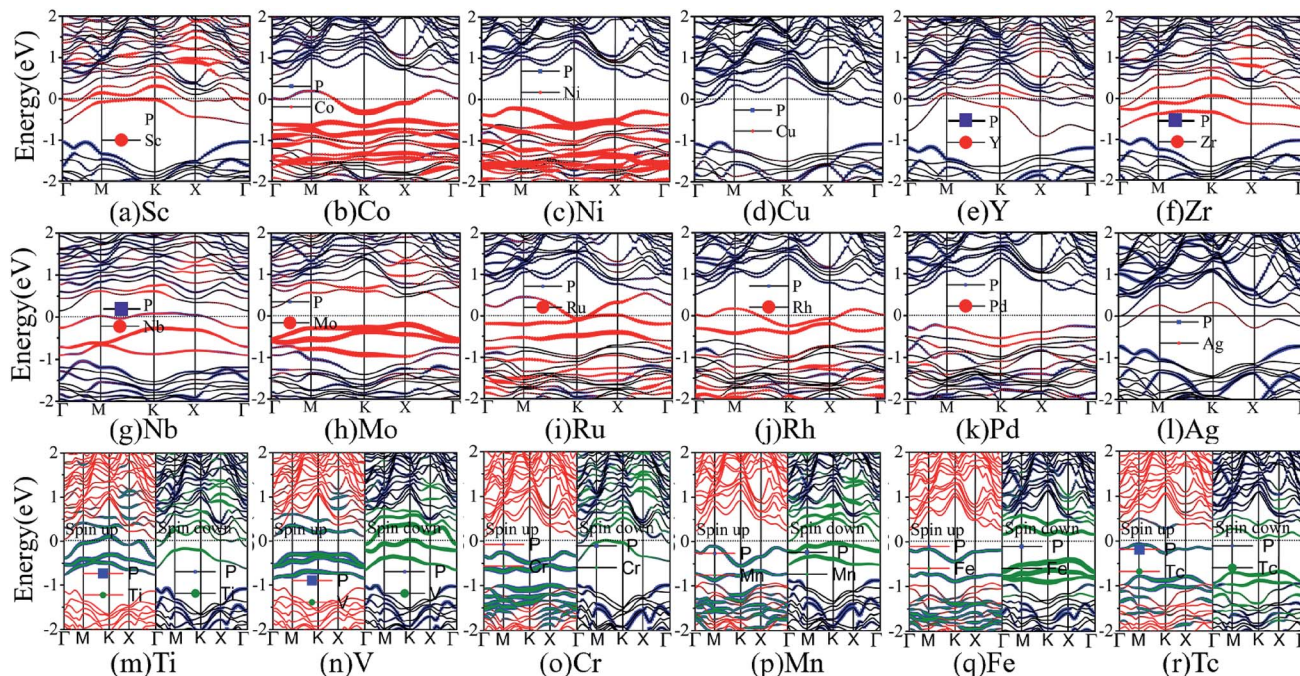
Fig. 10 The band structures of the various TM–BP/Tl$_2$S systems: (a) Sc-BP/Tl$_2$S, (b) Co-BP/Tl$_2$S, (c) Ni-BP/Tl$_2$S, (d) Cu-BP/Tl$_2$S, (e) Y-BP/Tl$_2$S, (f) Zr-BP/Tl$_2$S, (g) Nb-BP/Tl$_2$S, (h) Mo-BP/Tl$_2$S, (i) Ru-BP/Tl$_2$S, (j) Rh-BP/Tl$_2$S, (k) Pd-BP/Tl$_2$S, (l) Ag-BP/Tl$_2$S, (m) Ti-BP/Tl$_2$S, (n) V-BP/Tl$_2$S, (o) Cr-BP/Tl$_2$S, (p) Mn-BP/Tl$_2$S, (q) Fe-BP/Tl$_2$S, (r) Tc-BP/Tl$_2$S.

4. Conclusion

In conclusion, we have systematically researched the structural, electronic, and magnetic properties of the BP/Tl$_2$S and the BP/Tl$_2$S with intercalated various TMs by using first-principles calculations. The electronic structure results reveal that the CBM and the VBM of the BP/Tl$_2$S are uniquely dominated by the Tl$_2$S layer of the BP/Tl$_2$S, forming a type-I heterostructure with indirect band gap. Moreover, the band gaps of the BP/Tl$_2$S can be acutely modulated by uniaxial or biaxial uniform strain. The results show that the band gap is more sensitive to biaxial uniform strain than to uniaxial strain. There are the common features that the band gap of the BP/Tl$_2$S experiences an indirect–direct transition regardless of applying uniaxial or biaxial uniform strain. A more interesting thing is that the BP/Tl$_2$S undergoes transitions from type-I to type-II when various strain is applied. Furthermore, in order to enrich and induce the meaningful electronic and magnetic properties of the BP/Tl$_2$S, the BP/Tl$_2$S with intercalated various TMs in the interlayer is studied. Our results show that the electronic and magnetic properties of BP/Tl$_2$S can be widely tuned by TMs intercalated. In all TM–BP/Tl$_2$S systems, there are only six TM–BP/Tl$_2$S (Ti-, V-, Cr-, Mn-, Fe-, Tc-) systems showing robust ferromagnetism. We find the prominent change of the electronic structure induced by TMs intercalated as following: three TM–BP/Tl$_2$S (V-, Cr-, Mn-) systems show a half-metallic nature with 100% spin polarization. The Fe-BP/Tl$_2$S and Tc-BP/Tl$_2$S systems are DMSs. In six TM–BP/Tl$_2$S (Ti-, V-, Cr-, Mn-, Fe-, Tc-) magnetic systems, the Ti-BP/Tl$_2$S system is exception, which shows metallic character. In TM–BP/Tl$_2$S non-magnetic systems, only TM–BP/Tl$_2$S (Mo-, Pd-,

Ni-) systems are semiconductors. The other TM–BP/Tl$_2$S systems become metal. The results of the BP/Tl$_2$S and TM–BP/Tl$_2$S systems not only provide experimentally an effective route for designing novel two-dimensional material, but also may present good opportunities for application of the BP/Tl$_2$S and TM–BP/Tl$_2$S in flexible electronics and optoelectronics.

Conflicts of interest

There are no conflicts to declare.

Acknowledgements

References

1 J. E. Padilha, A. Fazzio and A. J. R. da Silva, *Phys. Rev. Lett.*, 2015, **114**, 066803.

2 N. B. Le, T. D. Huan and L. M. Woods, *ACS Appl. Mater. Interfaces*, 2016, **8**, 6286–6292.

3 W. Yu, Z. Zhu, S. Zhang, X. Cai, X. Wang, C.-Y. Niu and W.-B. Zhang, *Appl. Phys. Lett.*, 2016, **109**, 103104.

4 L. Huang, Y. Li, Z. Wei and J. Li, *Sci. Rep.*, 2015, **5**, 16448.

5 L. Huang, N. Huo, Y. Li, H. Chen, J. Yang, Z. Wei, J. Li and S.-S. Li, *J. Phys. Chem. Lett.*, 2015, **6**, 2483–2488.

6 Y. Deng, Z. Luo, N. J. Conrad, H. Liu, Y. Gong, S. Najmaei, P. M. Ajayan, J. Lou, X. Xu and P. D. Ye, *ACS Nano*, 2014, **8**, 8292–8299.

7 G.-H. Lee, Y.-J. Yu, X. Cui, N. Petrone, C.-H. Lee, M. S. Choi, D.-Y. Lee, C. Lee, W. J. Yoo, K. Watanabe, T. Taniguchi, C. Nuckolls, P. Kim and J. Hone, *ACS Nano*, 2013, **7**, 7931–7936.

8 S. Wang, X. Wang and J. H. Warner, *ACS Nano*, 2015, **9**, 5246–5254.

9 R. Gillen, J. Robertson and J. Maultzsch, *Phys. Rev. B: Condens. Matter Mater. Phys.*, 2014, **90**, 075437.

10 Z. Huang, X. Qi, H. Yang, C. He, X. Wei, X. Peng and J. Zhong, *J. Phys. D: Appl. Phys.*, 2015, **48**, 205302.

11 Q. Li, L. Xu, K.-W. Luo, L.-L. Wang and X.-F. Li, *Mater. Chem. Phys.*, 2018, **216**, 64–71.

12 H. V. Phuc, N. N. Hieu, B. D. Hoi and C. V. Nguyen, *Phys. Chem. Chem. Phys.*, 2018, **20**, 17899–17908.

13 H. Liu, Z. Huang, G. Wu, Y. Wu, G. Yuan, C. He, X. Qi and J. Zhong, *J. Mater. Chem. A*, 2018, **6**, 17040–17048.

14 L. Li, Y. Yu, G. J. Ye, Q. Ge, X. Ou, H. Wu, D. Feng, X. H. Chen and Y. Zhang, *Nat. Nanotechnol.*, 2014, **9**, 372–377.

15 H. Liu, A. T. Neal, Z. Zhu, Z. Luo, X. Xu, D. Tománek and P. D. Ye, *ACS Nano*, 2014, **8**, 4033–4041.

16 S. P. Koenig, R. A. Doganov, H. Schmidt, A. H. Castro Neto and B. Özyilmaz, *Appl. Phys. Lett.*, 2014, **104**, 103106.

17 S. Das, W. Zhang, M. Demarteau, A. Hoffmann, M. Dubey and A. Roelofs, *Nano Lett.*, 2014, **14**, 5733–5739.

18 W. Hu and J. Yang, *Comput. Mater. Sci.*, 2016, **112**, 518–526.

19 Y. Cai, G. Zhang and Y.-W. Zhang, *J. Phys. Chem. C*, 2015, **119**, 13929–13936.

20 N. Gillgren, D. Wickramaratne, Y. Shi, T. Espiritu, J. Yang, J. Hu, J. Wei, X. Liu, Z. Mao, K. Watanabe, T. Taniguchi, M. Bockrath, Y. Barlas, R. K. Lake and C. Ning Lau, *2D Mater.*, 2014, **2**, 011001.

21 L. Huang and J. Li, *Appl. Phys. Lett.*, 2016, **108**, 083101.

22 K. Lee, S. W. Kim, Y. Toda, S. Matsuishi and H. Hosono, *Nature*, 2013, **494**, 336.

23 A. Walsh and D. O. Scanlon, *J. Mater. Chem. C*, 2013, **1**, 3525–3528.

24 T. Inoshita, S. Jeong, N. Hamada and H. Hosono, *Phys. Rev. X*, 2014, **4**, 031023.

25 Q. Wu, J.-J. Zhang, P. Hao, Z. Ji, S. Dong, C. Ling, Q. Chen and J. Wang, *J. Phys. Chem. Lett.*, 2016, **7**, 3723–3729.

26 N. Song, Y. Wang, W. Yu, L. Zhang, Y. Yang and Y. Jia, *Appl. Surf. Sci.*, 2017, **425**, 393–399.

27 S. Shen, Y. Liang, Y. Ma, B. Huang, W. Wei and Y. Dai, *Phys. Chem. Chem. Phys.*, 2018, **20**, 14778–14784.

28 A. Andersen, S. M. Kathmann, M. A. Lilga, K. O. Albrecht, R. T. Hallen and D. Mei, *J. Phys. Chem. C*, 2012, **116**, 1826–1832.

29 S. Sattar, N. Singh and U. Schwingenschlögl, *ACS Appl. Mater. Interfaces*, 2018, **10**, 4266–4270.

30 Y. Gong, H. Yuan, C.-L. Wu, P. Tang, S.-Z. Yang, A. Yang, G. Li, B. Liu, J. van de Groep, M. L. Brongersma, M. F. Chisholm, S.-C. Zhang, W. Zhou and Y. Cui, *Nat. Nanotechnol.*, 2018, **13**, 294–299.

31 Y. Guang, Y. Yanmin, M. Hongran, M. Xiujuan, L. Congcong, L. Jie, Z. Qiang, Z. Zhidong, Y. Fuxing and L. Jia, *Nanotechnology*, 2018, **29**, 115201.

32 G. Kresse and J. Hafner, *Phys. Rev. B: Condens. Matter Mater. Phys.*, 1993, **47**, 558–561.

33 G. Kresse and J. Hafner, *Phys. Rev. B: Condens. Matter Mater. Phys.*, 1994, **49**, 14251–14269.

34 G. Kresse and J. Furthmüller, *Phys. Rev. B: Condens. Matter Mater. Phys.*, 1996, **54**, 11169.

35 J. Klimeš, D. R. Bowler and A. Michaelides, *J. Phys.: Condens. Matter*, 2009, **22**, 022201.

36 J. Klimeš, D. R. Bowler and A. Michaelides, *Phys. Rev. B: Condens. Matter Mater. Phys.*, 2011, **83**, 195131.

37 N. Song, H. Ling, Y. Wang, L. Zhang, Y. Yang and Y. Jia, *J. Solid State Chem.*, 2019, **269**, 513–520.

38 W.-B. Zhang, Q. Qu, P. Zhu and C.-H. Lam, *J. Mater. Chem. C*, 2015, **3**, 12457–12468.

39 J. P. Perdew, K. Burke and M. Ernzerhof, *Phys. Rev. Lett.*, 1996, **77**, 3865–3868.

40 Y. Li, S. Yang and J. Li, *J. Phys. Chem. C*, 2014, **118**, 23970–23976.

41 X. Han, H. Morgan Stewart, S. A. Shevlin, C. R. A. Catlow and Z. X. Guo, *Nano Lett.*, 2014, **14**, 4607–4614.

42 G. Giester, C. L. Lengauer, E. Tillmanns and J. Zemann, *J. Solid State Chem.*, 2002, **168**, 322–330.

43 M. Sun, J.-P. Chou, J. Yu and W. Tang, *Phys. Chem. Chem. Phys.*, 2017, **19**, 17324–17330.

44 C. He, M. Cheng and W. Zhang, *Mater. Res. Express*, 2018, **5**, 065059.

45 M. M. Dong, C. He and W. X. Zhang, *J. Mater. Chem. C*, 2017, **5**, 3830–3837.

46 J. Qiao, X. Kong, Z.-X. Hu, F. Yang and W. Ji, *Nat. Commun.*, 2014, **5**, 4475.

47 M.-Q. Long, L. Tang, D. Wang, L. Wang and Z. Shuai, *J. Am. Chem. Soc.*, 2009, **131**, 17728–17729.

48 X. Peng, Q. Wei and A. Copple, *Phys. Rev. B: Condens. Matter Mater. Phys.*, 2014, **90**, 085402.

49 Z. Zhang, X. Zou, V. H. Crespi and B. I. Yakobson, *ACS Nano*, 2013, **7**, 10475–10481.

50 D. W. Boukhvalov and M. I. Katsnelson, *Nano Lett.*, 2008, **8**, 4373–4379.

51 E. Kan, H. Xiang, F. Wu, C. Lee, J. Yang and M.-H. Whangbo, *Appl. Phys. Lett.*, 2010, **96**, 102503.

52 L. Ming-Yang, C. Qing-Yuan, H. Yang, L. Ze-Yu, C. Chao and H. Yao, *Nanotechnology*, 2018, **29**, 095203.

53 V. O. Özçelik, D. Kecik, E. Durgun and S. Ciraci, *J. Phys. Chem. C*, 2015, **119**, 845–853.

54 E.-j. Kan, Z. Li, J. Yang and J. G. Hou, *J. Am. Chem. Soc.*, 2008, **130**, 4224–4225.

55 Y. Wang and H.-P. Cheng, *Phys. Rev. B: Condens. Matter Mater. Phys.*, 2011, **83**, 113402.

56 X. Zhang, Z. Bao, X. Ye, W. Xu, Q. Wang and Y. Liu, *Nanoscale*, 2017, **9**, 11231–11238.

57 V. V. Kulish, O. I. Malyi, C. Persson and P. Wu, *Phys. Chem. Chem. Phys.*, 2015, **17**, 992–1000.

58 G. Henkelman, A. Arnaldsson and H. Jonsson, *Comput. Mater. Sci.*, 2006, **36**, 354–360.